

Driving complex flow waveforms with a linear voice coil actuator

Cite as: Biomicrofluidics 13, 034101 (2019); doi: 10.1063/1.5086286

Submitted: 19 December 2018 · Accepted: 19 April 2019 ·

Published Online: 3 May 2019



View Online



Export Citation



CrossMark

Dylan C. Young, Jacob M. Brehm, and Jan Srimgeour^{a)}

AFFILIATIONS

Department of Physics, Clarkson University, Potsdam, New York 13699, USA

^{a)}Electronic mail: jsrimge@clarkson.edu.

ABSTRACT

Oscillatory and pulsatile fluid flows for use in microfluidic applications were generated using a deformable chamber driven by a low cost linear voice coil actuator. Compliance in the fluidic system originating in the deformable chamber and the fluidic tubing produced a strong frequency dependence in the relationship between the system's input and the output flow rate. The effects of this frequency dependence were overcome by precise system calibration, enabling on-demand generation of sinusoidal oscillations in the fluid flow rate with a controlled amplitude in the range from 0.1 to over 1 ml/min across a frequency range from 0.1 Hz to 10 Hz. The calibration data further enabled the optimization of a multistage exponential smoothing model of the system that allowed the generation of arbitrary complex waveforms. This was demonstrated by combining flow modulation with a constant background flow generated by a syringe pump to mimic the pulsatile flow found in the human vascular system.

Published under license by AIP Publishing. <https://doi.org/10.1063/1.5086286>

I. INTRODUCTION

Oscillatory and pulsatile fluid flows are a common feature of natural and living systems. As a result, there is considerable interest in generating complex flows for a wide range of applications, including the study of biofilm formation and cellular behaviors such as bone maintenance, stem cell differentiation, and vascular health.^{1–6} Vascular health is of particular importance in the human body where endothelial cells are directly and continuously exposed to the blood flow at the vessel wall. These cells are integral to the integrity of the vascular system, but successful culture of these cells outside the body has been shown to depend on their exposure to the fluid flow, with even the nature of the complex fluid flow waveform playing an essential role in the maintenance of the endothelial phenotype.^{7,8} However, the generation of precisely controlled fluid flows can be technically challenging and costly.

Many different approaches have been taken to address these issues. Early systems for the generation of controlled pulsatile flow relied on traditional hydraulic approaches, using motor driven pistons to produce controlled variation in flow.⁹ More recently, it has become common to achieve flow manipulation via a deformable chamber situated within a fluidics system.^{10–17} In this case, the main choice for the researcher is the method of actuation that is used in conjunction with the chamber, and systems are commonly

driven via pneumatics, embedded magnets, or piezoelectric actuators.

One alternative approach for achieving precisely controlled actuation of a deformable chamber is the voice coil actuator (VCA). VCAs make use of the basic technology found in loudspeakers to produce precisely controlled linear motion. They have the advantage of being able to generate high forces and operate over long travel ranges and high frequencies. These actuators have been used previously in a more traditional hydraulic system to drive rigid pistons and have been used to generate defined pressure waveforms and pulsatile flow.^{18,19} Their use has also been demonstrated in systems with deformable chambers, but this was limited to the generation of sinusoidal fluid flow waveforms.²⁰ These flow waveforms were used to characterize the mechanical properties of fluidic systems, and this work highlights an important challenge faced in the generation of more complex flow waveforms. Specifically, systems with significant compliance, which might derive from the deformable chamber or the surrounding fluidic system, produce a frequency dependent damping of oscillatory fluid flows that must be accounted for to produce a defined output from such a system.

In this paper, we describe the optimization of a VCA-based system to generate complex fluid flow waveforms in the presence of

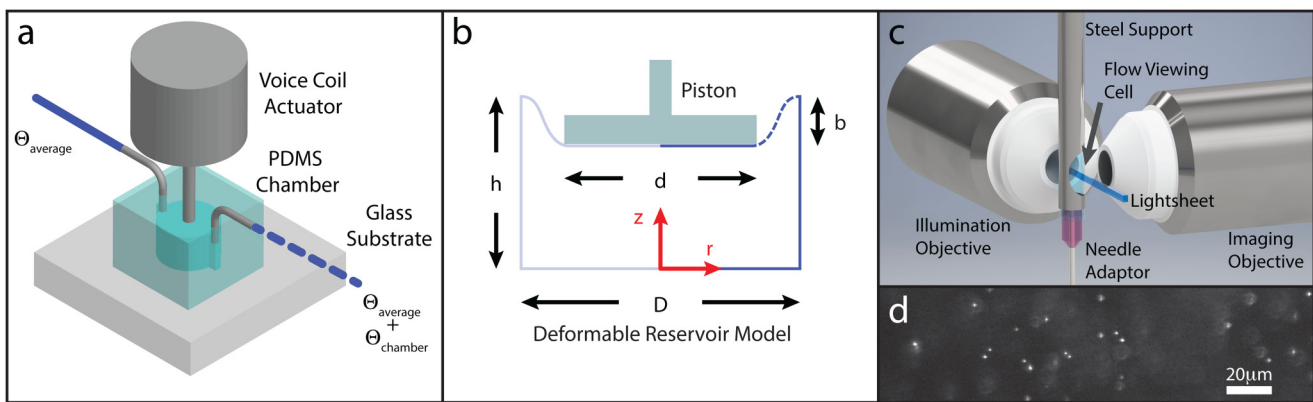


FIG. 1. (a) Schematic of the deformable chamber and voice coil actuator. (b) Schematic of the deformable chamber geometry. (c) Schematic of the lightsheet imaging system and the flow visualization cell used for particle image velocimetry of flows driven by the voice coil actuator. (d) Typical image from the microsphere suspension in the flow viewing cell.

the frequency dependent damping that arises from the mechanical properties of the deformable chamber, the elasticity within the fluidic system, and the actuator's control electronics. Through precise calibration and a multistage exponential smoothing model that accounts for the strong history dependence in the fluid flow rate, we demonstrate the precise generation of sinusoidal fluid flows, before combining flow modulation with the background flow generated by a syringe pump to mimic the pulsatile flow found in the blood stream. The system presented achieves this using readily accessible technologies, such as soft lithography and off the shelf components. The combination of the VCA and a deformable chamber, as illustrated in Fig. 1(a), allows precise modifications to be made to the flow rate through the fluidic system. This approach provides a flexible and reasonably low cost means of generating controlled, time varying, fluid flows and the technology that is highly scalable with a wide range of linear VCAs available to access a wide range of flow rates.

II. METHODS

A. Microfluidic system fabrication and assembly

The deformable chamber was fabricated by soft lithography from a thermoplastic master generated using stereolithography (Protolabs).²¹ Polydimethylsiloxane, PDMS (Silgard 184, Dow Corning), was mixed in the ratio 5:1 base to the curing agent and degassed under vacuum before it was poured into the thermoplastic mold leaving the upper surface of the mold cover in the thin layer of PDMS. It was then baked at 90 °C for 90 min. The resulting PDMS chamber was secured to a glass substrate by plasma bonding (Harrick Plasma, Expanded Plasma Cleaner) with both parts exposed to air plasma for 30 s prior to bonding under pressure at 90 °C for 45 min. The upper membrane thickness of several devices was measured and a device was selected with a membrane thickness of approximately 100 μm. Tubing (Cole-Palmer, 18 gauge PTFE) was inserted into the entry and exit ports of the chamber, and the whole system was clamped into the place with the deformable membrane

under the piston of the VCA (BEI Kimco, LAS13-18-000A-P01-3E). The end of the piston was modified with an M3 thread and a machined aluminum plunger was attached to the piston. The VCA used here has a 6 mm stroke, which can generate forces of up to 15 N, and can operate at frequencies up to 100 Hz. A schematic of the chamber is shown in Fig. 1(b) and the dimensions of the plunger and chamber used in this work are shown in Table I. A pressure sensor (40PC001B2A, Honeywell) was incorporated into the system immediately following the deformable chamber using a T-junction (P-712, IDEX corporation). Once the system is calibrated (as described below), the pressure sensor allows the performance of the system to be monitored in real time without further need for direct visualization of the fluid flow.

B. System control

Proportional-integral-derivative (PID) control of the VCA was enabled by a digital servo drive and a microcontroller (Pluto, Ingenia). In contrast to previous work,²⁰ this system enables precise control over the position of the VCA's piston rather than the driving current. In doing so, it enables complex motion of the piston, but sacrifices some knowledge of VCA's behavior, such as the force generated over time. Input waveforms were generated using a multifunction data acquisition (DAQ) device (6002, National Instruments) via custom code written in Python. The analog output from the DAQ was connected to the microcontroller's

TABLE I. Dimensions of the deformable chamber as detailed in Fig. 1(b).

Parameter	Dimension (mm)
Diameter, D	12.7
Height, h	6.35
Plunger diameter, d	4
Membrane depression, b	2–4

analog input and the applied voltage was used to control the position of the VCA plunger as function of time, $b(t)$. The parameters of the PID feedback loop were optimized *in situ* using the MotionLAB software (Ingenia), with the VCA mounted on the deformable chamber and the flow system flooded with water. The signal from the VCA's position encoder was recorded by the DAQ, enabling realtime monitoring of the piston position.

C. Flow visualization

To enable the visualization of fluid flow in the required range of flow rates (0.1–1 ml/min), a special viewing cell was constructed within the flow system, which is shown in Fig. 1(c). This consisted of 3 mm inner diameter, thin walled, FEP tubing (Norell), supported by a housing of steel tubing (McMaster). A notch was machined out of the steel housing to allow optical access to the flow system. 18 Gauge needles (Amazon Supply) were customized to act as adapters between the FEP and PTFE tubing. Once assembled, all joints in the flow system were sealed with epoxy to prevent leaks and accumulation of gas within the system.

Particle image velocimetry (PIV) was used to characterize the fluid flow generated by the deformable chamber.²² PIV was performed on a custom-built lightsheet microscope modeled on the open source OPENSPIM design.²³ Briefly, the sample, in this case water containing a dilute suspension of 0.5 μm yellow-green Fluospheres (Life Technologies), was illuminated and imaged using orthogonal water dipping objectives (Nikon 10× 0.3 NA—illumination; Nikon 16× 0.85 NA—imaging). Laser illumination at 488 nm (Vortran, Stradus 488-150) was formed into a lightsheet 400 μm tall and 3 μm deep using a cylindrical lens. Sample position was controlled by a 4-axis (x , y , z , and θ) micropositioning stage [Physik Instruments, M-110 (x and z -axes), M-111 (y -axis), M-116 (θ -axis), and C-884.4DC (controller)]. Imaging was performed using a sCMOS camera (Andor, Neo). Image series for analysis by PIV were recorded at 185 frames per second using the micromanager software.²⁴ PIV analysis was performed in ImageJ using a PIV plugin.^{25,26} PIV

was performed in the plane passing through the center of the viewing cell, allowing the measurement of the peak flow velocity through the cell. The peak volume flow rate, Θ was then calculated from the peak flow velocity, v_{flow} , assuming a parabolic velocity profile in the cylindrical chamber as $\Theta = \pi R^2 v_{flow}/2$. Flow in the system was assumed to be laminar given that the Reynolds number was approximately 2.

III. RESULTS AND DISCUSSION

A. System characterization

Expectations for the system's output were generated by assuming that the fluid was incompressible and all components of the system were rigid. In such a model system, the output flow rate $\Theta_{system} = \Theta_{average} + \Theta_{chamber}$, where $\Theta_{Average}$ is driven by a syringe pump and $\Theta_{chamber}$ simply depends on the velocity of the piston, $v_{piston} = db/dt$ and its effective area, A_{eff} so that $\Theta_{chamber} = v_{piston}A_{eff}$. The effective area of the plunger, which accounts not just for the area of the plunger, but also for the complex shape of the deforming membrane, was measured experimentally by moving the plunger at a constant speed of 0.058 mm/s. The volume flow rate in the system during this motion was measured using the lightsheet PIV, giving a value of 0.231 ml/min and setting the effective area of the piston at 66.1 mm². This is just slightly higher than expected from the machined radius of the VCA driven plunger.

The application of sinusoidal waveforms to the input of the system, however, make it clear that the system's behavior is far from ideal. Figure 2(a) shows the system's response, both VCA piston motion and the output flow rate, for an input sinusoidal waveform with a frequency of 2 Hz. Each quantity has been converted into units of flow rate following the simple model for the system presented above from an ideal system. These plots show good signal translation between the input and the VCA drive, while pronounced damping and phase shift occur in the measured fluid flow.

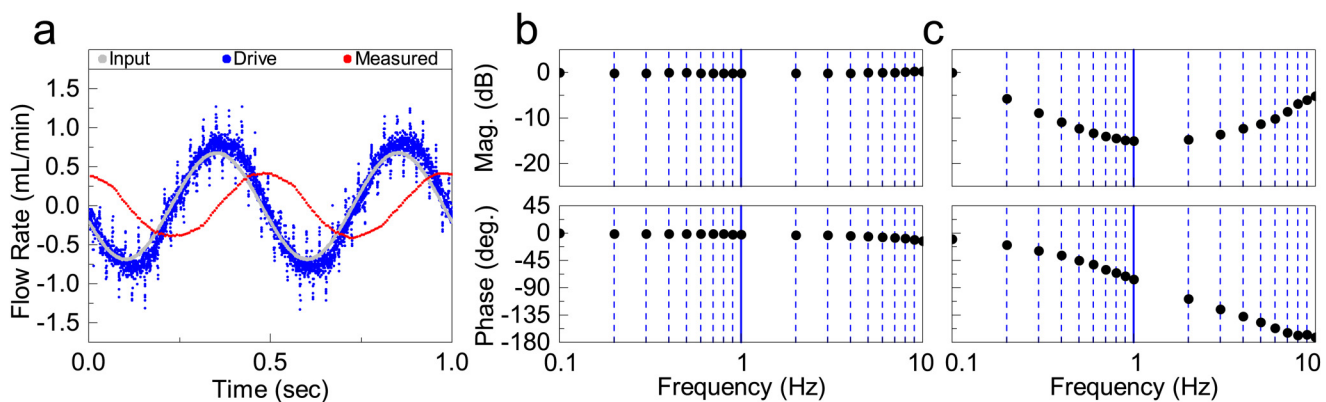
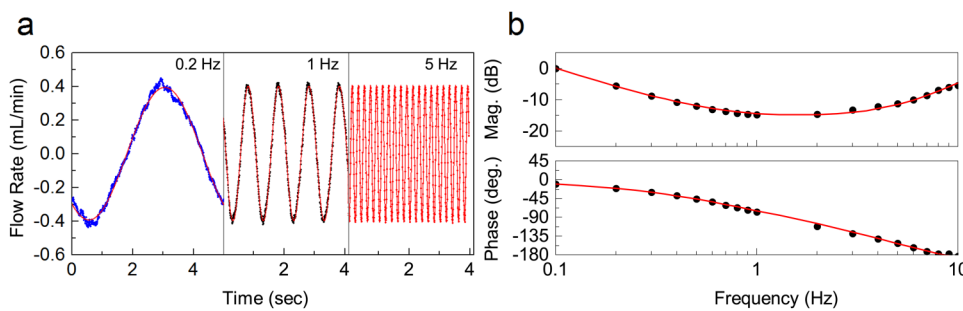


FIG. 2. (a) A real time comparison of VCA driving voltage, the position of the actuator's piston, and the associated fluid flow waveform for an input sinusoidal waveform with a frequency of 2 Hz. (b) Phase and amplitude plots for driving voltage and piston position. (c) Phase and amplitude plots for the piston velocity and fluid flow waveform.



Figures 2(b)–2(c) show Bode plots for two separate signal pairings in the system (i) input to piston position and (ii) piston velocity to flow rate. These plots indicate that the VCA's PID control system performs well over the frequency range studied with the motion of the piston closely following the input waveform. Meanwhile, the behavior of the flow system is more complex, with the measured flow rate proportional to the piston velocity at 0.1 Hz but exhibiting significant phase shifts and strong damping as the frequency increases. This behavior is largely a result of construction of the fluidic system, where the tubing, the syringe, and the drive chamber itself are made of flexible elastomers, and the resulting compliance in the system produces frequency dependent damping observed in the output waveform. Here, the compliance initially causes the system to behave like a lowpass filter; however, as the frequency of the flow waveform increases an upturn is observed in the Bode plot. This upturn was only observed when a component with a high fluidic resistance was placed in the outflow path from the deformable chamber (in this case, the T-junction used to incorporate the pressure sensor). With a low output resistance, no upturn in the amplitude was observed with increasing frequency.

The behavior of the system did not depend on the magnitude of the input amplitude, and the Bode plots were used as a calibration for the system, enabling the generation of sinusoidal waveforms with a precisely controlled peak flow rate. **Figure 3(a)** shows the controlled generation of three sinusoidal waveforms with frequencies of 0.2, 1, and 5 Hz with an amplitude of 0.4 ml/min. Good consistency in the amplitude of each waveform was observed and was replicated across the whole two decades of frequency investigated with the average flow rate across all waveforms of 0.406 ml/min with a standard deviation of 0.007 ml/min.

B. Empirical model

Initial testing of complex waveform generation revealed that the system's response is nonlinear and depends strongly on the recent flow history. Such effects can often be modeled by exponential smoothing. Guided by the Bode plots in **Figs. 2(b)–2(c)**, we choose to use 3-stage exponential smoothing to model the end-to-end behavior of the system.²⁷ This model has the lowest level of complexity that is capable of delivering the large phase shift observed over the two decade frequency range. The input to the smoothing function Θ_n^0 was calculated as the first derivative of the time-series describing the requested piston positions, b_n , multiplied by the effective area of the

FIG. 3. (a) Sinusoidal fluid flow waveforms with programmed amplitude of 0.4 ml/min at three frequencies. Lines are sinusoidal fits to the data. (b) Comparison between the end-to-end Bode plot for the fluidic system (dots) with the optimized 3-stage exponential smoothing model (solid lines).

piston, A_{eff} ,

$$\Theta_n^0 = \frac{b_n - b_{n-1}}{\Delta T^0} A_{eff}, \quad (1)$$

where the subscripts denote the position of data in each time series. Each stage of the smoothing function is then described as follows:

$$\Theta_n^{k+1} = a^k \Theta_{n-1}^{k+1} + (1 - a^k) \Theta_n^k, \quad (2)$$

where the superscripts denote the order in which the smoothing functions are applied, in this case $k = 0, 1, 2$, and a is the smoothing parameter. In preparation for each smoothing stage, we set $\Theta_0^{k+1} = \Theta_0^k$ and interpolated the time series so that the time interval between samples was ΔT^k . Periodic boundary conditions were used to generate periodic waveforms for comparison with the system's Bode plots.

The time delay and smoothing parameter for each filter stage were optimized by fitting the Bode plots for end-to-end transmission through the system (input to flow rate) and are shown in **Table II**. The model's performance was assessed by comparing Θ_n^3 , the final output from the optimized model, with the system's Bode plot, **Fig. 3(b)**. This multiple stage smoothing process accounts for the behavior of the control electronics, VCA, deformable chamber, and the extended fluidics system in determining the output of the system. In this case, the time constant, $\tau_c \approx \Delta T/a$ of the filter's final stage appears to a good match for a simple model of the fluidic system, and can be estimated from the product of the drive system's measured compliance ($4.33 \times 10^{-12} \text{ m}^5/\text{N}$) and the calculated fluidic resistance of the outflow ($6.98 \times 10^{10} \text{ Pa s/m}$). The drive system comprised all the fluidic hardware prior to the outflow, i.e., the syringe, deformable chamber, pressure sensor, and connecting tubing. The compliance was measured by monitoring the pressure change in the system as the VCA piston was driven to produce a series of constant flow rates. The total fluidic resistance of the system was calculated as the sum of the fluidic resistance, R_f of each element in the system. Here, each element

TABLE II. Fitted parameters for three-stage exponential smoothing, as described by **Fig. 3(b)**.

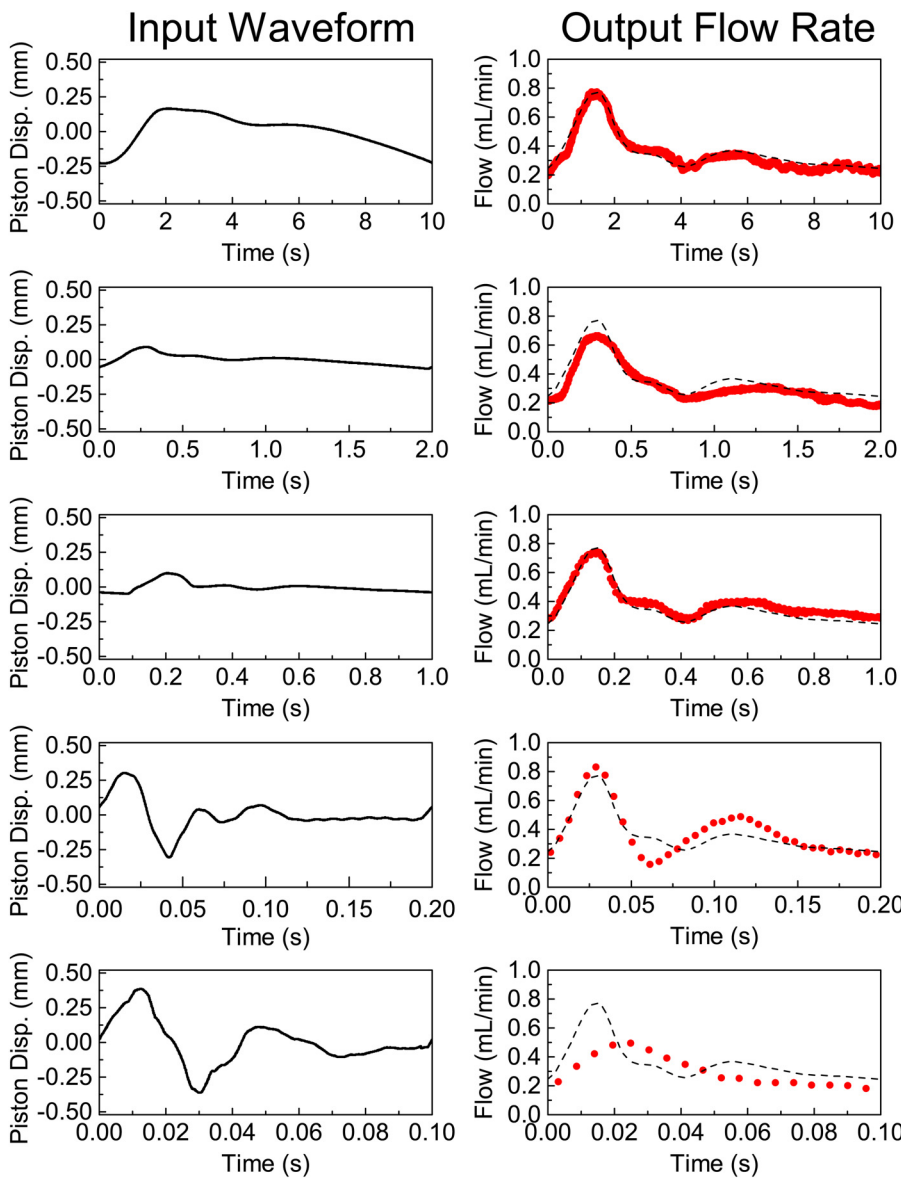
Smoothing order, k	0	1	2
Smoothing parameter, a^k	0.95846	0.99779	0.86658
Time delay, $\Delta T^k(\text{s})$	0.01051	0.000068	0.00318

in the system had a circular cross section and $R_f = 8\pi\eta L/A^2$, where η is the dynamics viscosity of the fluid, L is the length of an individual section of the tubing, and A is the local cross-sectional area.

C. Complex flow generation

Arbitrary flow waveforms may be generated in the fluidics system using the empirical model described in Sec. III B. This is accomplished by deconvolution of the desired output waveform to generate the necessary input. Each step in the deconvolution through the 3-stage smoothing process used the following equation:

$$\Theta_n^k = \frac{\Theta_n^{k+1} - a^{k+1}\Theta_{n-1}^{k+1}}{1 - a^{k+1}}. \quad (3)$$



The optimized parameters, described in Table II, were used in the reverse order for deconvolution, i.e., $k = 2, 1, 0$, since the process is noncommutative. Once Θ_n^0 , the required input flow rate, was obtained, it was integrated to generate $b(t)$, the time-series describing the required sequence of piston positions needed to produce the desired flow waveform

$$b_n = \frac{\Theta_n^0 - \Theta_{n-1}^0}{2A_{eff}} \Delta T^0 + b_{n-1}. \quad (4)$$

Here, we used $b_0 = 0$ to generate a set of relative positions that can be applied from an arbitrary piston starting position.

To demonstrate the systems ability to generate complex waveforms, the generation of a complex pulsatile flow that mimics the

FIG. 4. Generation of pulsatile fluid flows resembling those found in the human vascular system. The waveforms were reproduced at frequencies of 0.1, 0.5, 1, 5, and 10 Hz based on the three step filter model for the microfluidic system. The optimized input waveforms are shown in the left column, while the right column shows the target waveform (dashed lines) and measured output flow rates (dots).

flow found in a healthy human vascular system.⁸ This waveform was produced with an additional flow of 0.33 ml/min generated by the attached syringe pump so that the flow is unidirectional but varying in the flow rate. The input waveforms needed to generate the atheroprotective waveform over the range of frequencies from 0.1 to 10 Hz are shown in Fig. 4 along with the measured response of the system to these inputs. At the lowest frequency, the input waveform is a good approximation for the basic model where the flow rate is simply proportional to the piston velocity. At higher frequencies, input waveforms exhibit large deviations from this model. The output waveforms show excellent fidelity with the target through the frequency range 0.1 to 1 Hz. Beyond this, waveforms up to 5 Hz are good approximations to the desired output, but the fine features of the waveform are progressively lost as the frequency increases from 1 to 10 Hz. This effect is in large part due to the frequency range used in calibrating the system and optimizing the smoothing model. In essence, the model has no information about what happens at frequencies above 10 Hz; these frequencies are, however, important in the reproduction of the 5–10 Hz waveforms since they play an increasing role in their Fourier spectrum. We believe that this discrepancy would likely be overcome by characterization of the system over an extended frequency range.

IV. CONCLUSIONS

We have demonstrated the generation of complex fluid flow waveforms with a linear voice coil actuator driving a deformable fluidic chamber. Under dynamic modulation, strong history dependence was observed in the flow rate generated through the system, which was primarily a result of the compliance of the deformable chamber and elastic tubing used in the assembly of the fluidic system. Complex waveform generation was enabled by modeling the system's Bode plots using 3-stage exponential smoothing. This model accounted for the effects of the system's compliance as well as secondary sources of frequency dependence such as the system's drive electronics. The required input waveform needed to generate an arbitrary output could then be calculated by deconvolution. This work will pave the way for more precise generation of fluid flow waveforms in systems that exhibit moderate to strong history dependence due to their internal compliance and may be important in applications such as the microfluidic culture of living cells. We believe that further study and modeling of this system will enable the efficient generation of arbitrary complex waveforms over a wider frequency range. In addition, this approach is highly scalable with linear voice coil actuators available that can generate forces up to 1500 N to drive large volumes of fluid with high flow rates and frequencies.

REFERENCES

- ¹P. Stoodley, Z. Lewandowski, J. D. Boyle, and H. M. Lappin-Scott, *Biotechnol. Bioeng.* **65**, 83 (1999).
- ²C. Jacobs, C. Yellowley, B. Davis, Z. Zhou, J. Cimbala, and H. Donahue, *J. Biomech.* **31**, 969 (1998).
- ³Y. J. Li, N. N. Batra, L. You, S. C. Meier, I. A. Coe, C. E. Yellowley, and C. R. Jacobs, *J. Orthop. Res.* **22**, 1283 (2004).
- ⁴E. Stavenschi, M.-N. Labour, and D. A. Hoey, *J. Biomech.* **55**, 99 (2017).
- ⁵G. Helmlinger, R. Geiger, S. Schreck, and R. Nerem, *J. Biomech. Eng.* **113**, 123 (1991).
- ⁶O. Traub and B. C. Berk, *Arterioscler. Thromb. Vasc. Biol.* **18**, 677 (1998).
- ⁷B. R. Blackman, G. Garc-Cardena, and M. A. Gimbrone, *J. Biomech. Eng.* **124**, 397 (2002).
- ⁸G. Dai, M. R. Kaazempur-Mofrad, S. Natarajan, Y. Zhang, S. Vaughn, B. R. Blackman, R. D. Kamm, G. Garca-Cardea, and M. A. Gimbrone, *Proc. Natl. Acad. Sci. U.S.A.* **101**, 14871 (2004).
- ⁹D. Holdsworth, D. Rickey, M. Drangova, D. Miller, and A. Fenster, *Med. Biol. Eng. Comput.* **29**, 565 (1991).
- ¹⁰C. H. Yap, N. Saikrishnan, G. Tamilselvan, and A. P. Yoganathan, *Biomech. Model. Mechanobiol.* **11**, 171 (2012).
- ¹¹J. Shao, L. Wu, J. Wu, Y. Zheng, H. Zhao, Q. Jin, and J. Zhao, *Lab Chip* **9**, 3118 (2009).
- ¹²H. Chen, J. Cornwell, H. Zhang, T. Lim, R. Resurreccion, T. Port, G. Rosengarten, and R. E. Nordon, *Lab Chip* **13**, 2999 (2013).
- ¹³H.-Y. Tseng, C.-H. Wang, W.-Y. Lin, and G.-B. Lee, *Biomed. Microdevices* **9**, 545 (2007).
- ¹⁴A. Gaspar, M. E. Piyasena, L. Daroczi, and F. A. Gomez, *Microfluid. Nanofluidics* **4**, 525 (2008).
- ¹⁵J. Li, M. Zhang, L. Wang, W. Li, P. Sheng, and W. Wen, *Microfluid. Nanofluidics* **10**, 919 (2011).
- ¹⁶B. Zhao, X. Cui, W. Ren, F. Xu, M. Liu, and Z.-G. Ye, *Sci. Rep.* **7**, 11319 (2017).
- ¹⁷R. Jain and B. Lutz, *Lab Chip* **17**, 1552 (2017).
- ¹⁸R. A. Wahab, E. J. Neuberger, B. G. Lyeth, V. Santhakumar, and B. J. Pfister, *J. Neurosci. Methods* **248**, 16 (2015).
- ¹⁹C. F. Brake, "Design of a cardiovascular flow mimicking pump," M.S. thesis (Dalhousie University, 2016).
- ²⁰S. Vedel, L. H. Olesen, and H. Bruus, *J. Micromech. Microeng.* **20**, 035026 (2010).
- ²¹U. Mirsaidov, J. Scrimgeour, W. Timp, K. Beck, M. Mir, P. Matsudaira, and G. Timp, *Lab Chip* **8**, 2174 (2008).
- ²²C. E. Willert and M. Gharib, *Exp. Fluids* **10**, 181 (1991).
- ²³P. G. Pitrone, J. Schindelin, L. Stuyvenberg, S. Preibisch, M. Weber, K. W. Eliceiri, J. Huisken, and P. Tomancak, *Nat. Methods* **10**, 598 (2013).
- ²⁴A. D. Edelstein, M. A. Tsuchida, N. Amodaj, H. Pinkard, R. D. Vale, and N. Stuurman, *J. Biol. Methods* **1**, 39 (2014).
- ²⁵C. A. Schneider, W. S. Rasband, and K. W. Eliceiri, *Nat. Methods* **9**, 671 (2012).
- ²⁶Q. Tseng, E. Duchemin-Pelletier, A. Deshiere, M. Balland, H. Guillou, O. Filhol, and M. Thry, *Proc. Natl. Acad. Sci.* **109**, 1506 (2012).
- ²⁷R. P. Winters, *Manage. Sci.* **6**, 324 (1960).